J Therm Anal Calorim (2010) 102:907–913
DOI 10.1007/s10973-010-0898-2

CeO_2-catalyzed ozonation of phenol

The role of cerium citrate as precursor of CeO_2

M. F. Pinheiro da Silva · L. S. Soeira · K. R. P. Daghastanli · T. S. Martins · I. M. Cuccovia · R. S. Freire · P. C. Isolani

Received: 27 January 2010 / Accepted: 17 May 2010 / Published online: 3 June 2010

Abstract Three different cerium citrate-based precursors were used for synthesizing CeO_2 through thermal treatment. Three morphological types of CeO_2 were obtained. Characterization of these oxides was carried out by XRD patterns, SEM microscopy, N_2 adsorption isotherms, Raman spectroscopy, zeta potential, and UV/Vis luminescence. Ozonation of phenol catalyzed by CeO_2 was studied as a representative reaction of environmental interest. The differences on the catalytic activity showed by these three oxides could be correlated to amounts of Ce^{3+} on CeO_2 surface and, consequently, to the demand for oxygen needed to burn each precursor.

Keywords Cerium oxide · Polymeric precursors · Ozonation · Redox catalyst

Introduction

Much attention has been paid to rare earth compounds due to their importance in new materials [1–3]. Among these compounds, lanthanide oxides represent an interesting and rich field, due to their applications in catalysis [4], solid electrolytes [5], and medicine [6].

M. F. Pinheiro da Silva · L. S. Soeira · K. R. P. Daghastanli · I. M. Cuccovia · R. S. Freire · P. C. Isolani (✉)
Instituto de Química, Universidade de São Paulo, CP 26077, São Paulo, SP 05513-970, Brazil
e-mail: pcisolan@iq.usp.br

T. S. Martins
Departamento de Ciências Exatas e da Terra, Universidade Federal de São Paulo, São Paulo, SP, Brazil

CeO_2 is by far the most studied lanthanide oxide. Most of the useful properties of CeO_2 are derived from the energetic trade-off between the low redox potential of Ce^{3+}/Ce^{4+} and the thermal stability of its fluorite-type structure [7]. In normal conditions, a Ce^{3+} ion is more stable than Ce^{4+}. In CeO_2, fluorite structure, however, Ce^{4+} is the predominant redox state. The combination of structural stability and redox activity lowers the potential Ce^{3+}/Ce^{4+}, making CeO_2 a very good catalyst in redox reactions [8, 9].

The search for improving the desired properties of CeO_2 using modern microscopy techniques has resulted in the establishment of several methods to synthesis CeO_2 in well-characterized morphologies [10–14]. These morphologies have been exploited as electronic conducting materials [15], electrochemical systems [16], and catalysts [17, 18].

Degradation of environmental pollutants present in industrial effluents depends on development of efficient catalysts. In this way, ozonation represents a good technique for degrading pollutants [19, 20]. Ozone can degrade pollutants through two different pathways: ozone direct attack to organic compounds (direct reaction) or hydroxyl radical generation (indirect reaction). It has been pointed out that the direct reaction is quite inefficient in mineralizing organic pollutants, especially in acidic solutions [20, 21]. On the other hand, pollutant oxidation by $OH^{\bullet}$ radical is known to be effective and fast. Recent works have also showed that the metal oxides can increase ozone dissolution, catalyze radical generation, and consequently enhancing mineralization rates of organic pollutants [22, 23].

In this study, CeO_2, in three morphological forms, was used for catalytic ozonation of phenol. The correlation between properties of citrate-based precursors of oxides,

oxide morphologies, and their performances as catalysts for degradation of phenol through ozonation were evaluated.

Experimental details

Syntheses

Three citrate-based precursors were prepared. Cerium citrates [Ce(Cit)·xH_2O] and [$Ce_2(HCit)_3$·$2H_2O$], respectively, precursors I and II, were synthesized using the procedures which has been already published [24]. Precursor III [$Ce(Cit)_x(NO_3)_y$·$6H_2O$], was synthesized mixing 25 mL of solutions of 0.23 mol L^{-1} of $Ce(NO_3)_3$·$6H_2O$ and 0.17 mol L^{-1} citric acid (H_3Cit). The resulting solution was evaporated to dryness at 373 K and kept at that temperature for 5 h.

Calcination of the three precursors yielded CeO_2 I, II, and III. This preparation was carried out in alumina crucibles, in a furnace, under 50 mL min^{-1} air flux, with temperature increase of 10 K min^{-1}, up to 873 K and 1 h at the final temperature. All oxides were left to cool down to room temperature in a desiccator, under anhydrous $CaCl_2$ [14].

Characterizations

Characterization of precursors I and II were reported previously [24]. Precursor III was characterized by CHN elemental analysis and TG/DTA analysis. Cerium oxides were characterized by X-ray diffraction patterns (XRD), BET multipoint surface analysis, scanning electron microscopy (SEM) and Raman spectroscopy, zeta potential measurements at pH 3, and emission spectroscopy. Characterizations of oxide types 1 and 2 have been reported previously [14].

Thermogravimetric measurements were carried out in a TG/DTA Shimadzu model DTG-60/DTG-60A thermal analyzer. Typically, 10 mg of a sample was placed in a platinum crucible and 10 mg of ignited alumina was used as reference. A thermal program with heating rate of 10 K min^{-1}, in the temperature range 398–1473 K, in 50 L min^{-1} of atmospheric air flow was used.

XRD patterns of precursors and oxides were carried out using a diffractometer Rigaku® on a $\theta/2\theta$ geometry between 10° and 120° using counting times of 2 s per point for a step size of 0.05° (2θ) using Cu Kα ($\lambda = 0.1518$ nm) monochromatized radiation, operating at $I = 20$ mA, $V = 40$ kV. The Y_2O_3 standard was prepared by heating 99.99% purity Y_2O_3 (Aldrich) up to 1473 K with dwell time of 72 h at the maximum temperature. This was followed by slow cooling to room temperature for 36 h prior to the analyses. The XRD pattern of Y_2O_3 was collected in $\theta/2\theta$ geometry between 5° and 120°, counting time 5 s per point, for a step size of 0.02° (2θ).

Raman spectra of CeO_2 samples were recorded on a Renishaw model 3000 imaging system coupled to a He–Ne laser (Spectra Physics model 127, $\lambda = 632.8$ nm) equipped with an Olympus metallurgical microscope and a CCD detector. Crystallite size calculations through Raman spectroscopy were carried out by the phonon confinement model approach [25].

SEM images were recorded on a JEOL field emission scanning electron microscope, JSM 7401F, using a LEI detector. Oxide samples were previously recovered with 3 nm of Au on an Edwards Scancoat operating at 15 mA and 1.5 kV. Oxide crystallite size calculations through XRD patterns were performed using a Rietveld GSAS refining program, following pseudo-voight methods [26].

Surface area and pore size measurements were carried out on a Quantachrome analyzer Nova 1200e, through N_2 adsorption at 77 K using the BET and BJH models, respectively [27, 28]. Prior to measurements, oxide samples were degassed at 573 K under vacuum for 3 h.

Zeta potentials measurements of 1.5 mg L^{-1} of each morphological CeO_2, dispersed in aqueous 1 mM of H_2SO_4, pH 3, were carried out on an electrophoretic system (Malvern nanoseries) using a backlight scattering detector, following the Smoluchowski method [29].

Emission and excitation spectra of CeO_2 were recorded on a SPEX model 1934 D spectrofluorimeter at room temperature.

Catalytic tests

Oxide-catalyzed ozonation tests were performed in a tubular reactor with 300-mL capacity and ratio height/internal diameter equal to 5. Each catalytic test was carried out using 100 mg L^{-1} of phenol solution, pH 3 (1-mM H_2SO_4), with 100 mg L^{-1} of CeO_2 in one of the three morphologies. Ozone concentrations of ca. 32 mg L^{-1} were obtained, bubbling the mixture O_2/O_3 in the solution during 60 min, under 800-rpm magnetic stirring. Residual gas exhausted from the reactor was decomposed in a KI solution (2%), before releasing to the environment. Ozone monitoring was carried out at 258 nm with a Shimadzu spectrophotometer (Multi Spec-1501) with flow cell, 1-cm optical path. Aliquots were taken from the reactor at 2.5 and 5 min of reaction time and, from there on, at 10-min intervals until the end of experiments (Fig. 1).

TOC determinations were carried out in a Shimadzu TOC-5000A analyzer, using a standard method [30]. Colorimetric phenol determinations were carried out in a spectrophotometer (Femto model 700 S) at 510 nm, using also a standard method [31]. Ozone was generated using

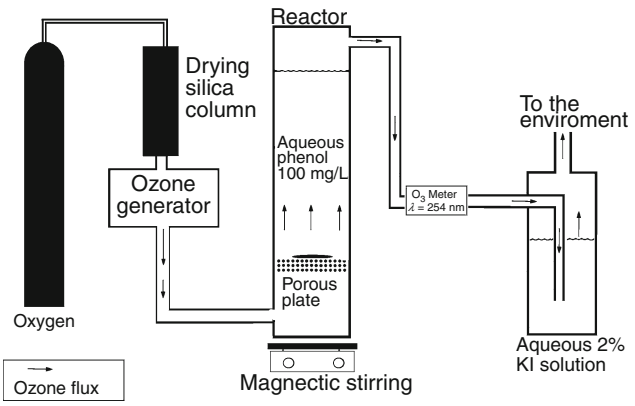

Fig. 1 Experimental setup utilized in heterogeneous catalyzed ozonation

dry O_2 (White Martins, 99,999%) as feeding gas for a corona generator Multivácuo (MV 06).

Results and discussions

Characterizations

Three morphological types of CeO_2 were synthesized through thermal treatment of three different cerium citrate-based precursors. Precursors and oxides I and II were synthesized and characterized previously [14, 24]. Elemental analysis of CHN of precursor III, $[Ce(Cit)_x(NO_3)_y{\cdot}6H_2O]$, showed 11% of nitrogen. For sake of clarity, precursor I has amorphous nature and stoichiometry $[Ce(Cit){\cdot}xH_2O]$, Cit = $(C_6O_7H_5)^{3-}$. Figure 2 shows SEM images of the three morphological CeO_2. SEM analysis of precursor I showed aggregates of irregularly shaped particles. Precursor II has crystalline nature and stoichiometry $[Ce_2(HCit)_3{\cdot}2H_2O]$, HCit = $(C_6O_7H_6)^{2-}$. SEM microscopy analysis evidenced its fibrous crystalline habit. After thermal treatment, the morphologies of precursors were hierarchically maintained, forming oxides with similar morphologies. Precursor III showed irregular aggregate morphology as well as CeO_2 III after calcination [14].

TG/DTG/DTA analysis of precursors I and II (not shown) showed similar one-step exothermic patterns of thermal decomposition with CeO_2 being formed at around 573 K as a consequence of the low redox potential (Ce^{+3}/Ce^{+4}) [21]. Precursor III showed a similar one-step exothermic pattern of decomposition, however, more exothermic than precursors I and II. It is reported in the literature [32] that this composition of precursor III, under calcination, generates temperatures around 1900 K, attributed to internal combustion at fuel-rich conditions (citrate/nitrate ratio > 0.8).

Rietveld plot of XRD patterns of CeO_2 I, II, and III are presented in Fig. 3. All these oxides showed well-defined fluorite structure with Fm3m space group (PDF#34-0394). Rietveld structural refinements of CeO_2 I and II showed that average crystallite sizes were, respectively, 20 and 21 nm, as shown in Table 1. Despite the fibrous character of CeO_2 II, XRD analysis could not detect any preferential orientation of crystallite growing. CeO_2 III shows a larger crystallite size, 35 nm, as a consequence of the higher temperature generated during internal combustion. That higher temperatures lead to formation of larger crystallites through sintering. Despite the fact that different amounts of Ce III are present on each of the synthesized oxides, their diffraction patterns remain almost unchanged. CeO_2 fluorite structure can lose oxygen (O^{2-}) generating an oxygen vacancy and two Ce III with no collapse of structure. Therefore, small amounts of Ce III on the surface and in the bulk do not cause appreciable changes in XRD patterns. This behavior allows the application of ceria as an oxygen storage material [15].

Average crystallite size calculations of the three morphological CeO_2 carried out by Rietveld structural refinement of XRD patterns agree reasonably well with those made through phonon confinement using Raman spectroscopy [25] (Table 1).

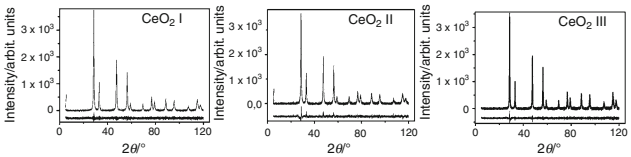

Fig. 3 XRD patterns of three synthesized CeO_2 as Rietveld

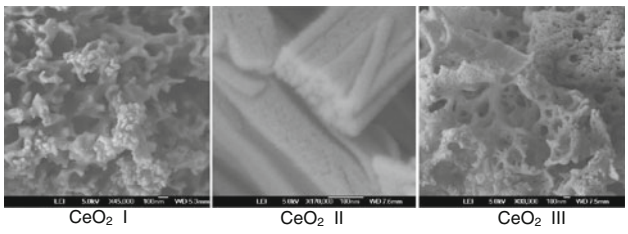

Fig. 2 SEM images of three synthesized CeO_2

Table 1 Results of crystallite size determinations from Raman and XRD

Oxide	Crystallite Size/nm	
	XRD	Raman
CeO_2 I	20	16
CeO_2 II	21	20
CeO_2 III	35	35

Table 2 K_{obs}, surface area, k_{area}, zeta potential (ζ_{pot}) and 1/zeta potential $(\zeta_{pot})^{-1}$

	K_{obs}	Surf. area/m^2 g^{-1}	K_{area} surf. area/m^{-2}	ζ_{pot}/mV	ζ_{pot}^{-1}/mV^{-1}
CeO_2 (I)	5.6×10^{-2}	18	3.1×10^{-3}	29 ± 3	3.4×10^{-2}
CeO_2 (II)	4.9×10^{-2}	8	5.1×10^{-3}	20 ± 3	5.0×10^{-2}
CeO_3 (III)	5.2×10^{-2}	54	1.4×10^{-3}	36 ± 3	2.7×10^{-2}

N_2 adsorption isotherms carried out onto CeO_2 I and II could be classified as Brunauer type III, which are characteristic of non-porous solids [33]. BET multipoint analysis, obtained from isotherms, showed that oxide type I has 18 m^2/g of surface area, CeO_2 II has 8 m^2g^{-1}, and CeO_2 III has 54 m^2g^{-1} (Table 2). Nanofiber morphology of CeO_2 II explains its lower surface area, while CeO_2 I does not have a structure as compact, as evidenced by SEM images. The N_2 isothermal adsorption of CeO_2 III shows a small hysteresis which evidences a porous character of CeO_2 III. This character is due to NO_3^- anion present in precursor III that at temperature around 300 °C decomposes, releasing large amounts of gas. These gases separate the particles from each other, creating inter-particular pores, increasing the surface area, as shown by SEM images [34]. Calculations of pore diameter by the BJH desorption method [33] show that pores have 17 nm of average diameter, compatible with typical interparticular pore sizes. In agreement with the identified hysteresis, surface area of CeO_2 III is also larger than the other two oxides.

Measurements of zeta potential, ζ_{pot}, of CeO_2 I, II, and III, suspended in H_2SO_4, at pH 3, showed that the surfaces are quite differently charged at the condition of experiments (Table 2), the order being CeO_2 III > CeO_2 I > CeO_2 II.

Figure 5 shows the UV/Vis luminescence spectra of the three oxides in the solid state. Band intensities were normalized by surface areas. All spectra show the transition 5d → 4f attributed to the Ce^{3+} ion. The order of values of band areas is: CeO_2 II > CeO_2 I > CeO_2 III (Fig. 4). Band areas may be related to surface concentrations of Ce^{3+} ions, since Ce^{4+} does not show luminescence at the experimental conditions [34].

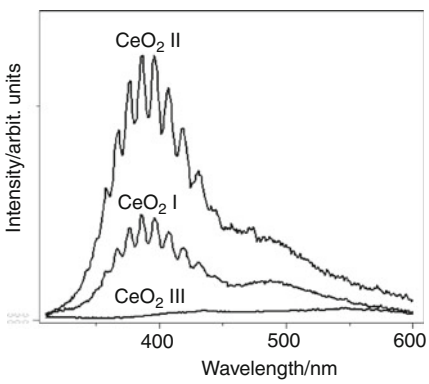

Fig. 4 Luminescence spectra of three CeO_2 as indicated in the figure $\lambda_{exc} = 280$ nm

Catalytic test

Catalytic ozonation tests using CeO_2 I, II, and III were performed using phenol. Figure 5 shows the phenol degradation and Fig. 6 shows the TOC removal during degradation. These figures allowed the identification of two steps in the ozonations: first, phenol degradation by dissolved ozone occurs; subsequently, degradation of by-products (BP) takes place.

After 10-min reaction time, phenol concentration was below the limit of detection of spectrophotometric analysis (0.5 mg L^{-1}). It was also verified that the presence of CeO_2, in any morphology, did not cause any appreciable change on the rate of phenol degradation, as shown in Fig. 5. Such behavior is an indicative that direct ozonation reaction is the predominant mechanism in the first step of phenol degradation.

The ozonation of BP until mineralization, however, was greatly improved, even using low amounts of CeO_2. TOC analysis, shown in Fig. 6, showed that all BP were

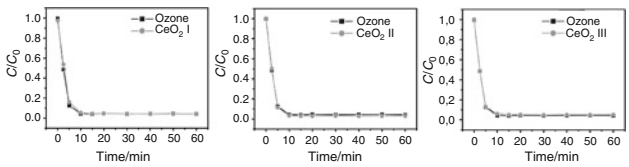

Fig. 5 Variation of phenol concentration as a function of ozonation treatment time (colorimetric analysis). Ozonation process using 100 mg L^{-1} of phenol, aqueous solution, pH 3, in the presence of ozone only and CeO_2 I, II, III

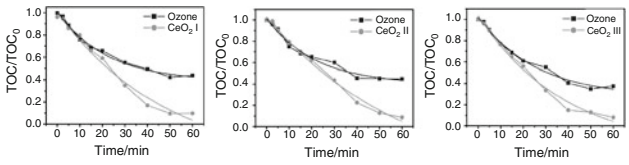

Fig. 6 Variation total organic carbon as a function of ozonation treatment time. Ozonation process using 100 mg L^{-1} of phenol, aqueous solution pH 3, in the presence of ozone only and CeO_2 I, II, III

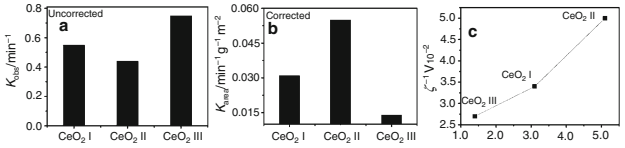

Fig. 7 Ozonation tests with CeO_2 1, 2 and 3: comparison of **a** K_{obs}, **b** k_{area}, and **c** plot of zeta potential against k_{area}

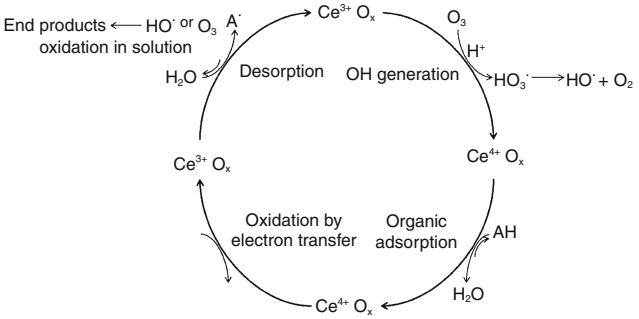

Fig. 8 Catalytic pollutant oxidation cycle

mineralized after 1 h of ozonation catalyzed by CeO_2. In the same conditions, ozone alone showed only 60% mineralization.

All mechanisms explaining oxide-catalyzed ozonation of pollutants in the literature consider adsorption of ozone and/or pollutant as the rate-determining step [35, 36]. It was verified, through adsorption assays, that phenol at concentration of 100 mg/L, pH 3 did not show appreciable adsorption on CeO_2. This suggests that at pH 3 aqueous phenol is quickly oxidized by dissolved ozone independently of CeO_2 [37]. This fact is in agreement with radical scavenger properties of CeO_2 and the short lifetime of radicals generated at the surface [6].

The ozonation of BP, however, showed high sensitivity to the presence of CeO_2 which was attributed to the adsorption of BP onto CeO_2 particle surfaces and radicals generated from ozone reduction in acid medium. According to Mvula and Sonntag [37] and Poznyk and Vivero [38], the major products of ozonation of phenol in pH $\leq$3 are: hydroquinone, cathecol, 1,4 benzoquinone, fumaric, maleic, oxalic, formic, and muconic acids. All these molecules adsorb very well onto positively charged CeO_2 surfaces, at pH 3 due to their carbonyl, hydroxyl, and carboxyl groups.

TOC monitoring of CeO_2-catalyzed ozonation of all catalytic tests showed that TOC decreases are almost equal during the first 20 min of ozonation. This time range stands for the already discussed phenol ozonation which did not show influence due to the presence of CeO_2.

For ozonation of SP, the pseudo-first-order kinetic constants (k_{obs}) were calculated using the equation $k_{obs} \cdot t = -\ln(TOC/TOC_o)$. Calculated k_{obs} for the three tested ozonations showed that activities of oxides followed the sequence CeO_2 II < CeO_2 I < CeO_2 III. The results are shown in Fig. 7a. It is known that k_{obs} depends on surface areas. Thus, correcting k_{obs} for the catalysts' surface areas, the order of activity observed (k_{area}) was CeO_2 II > CeO_2 I > CeO_2 III. This points out the best performance of CeO_2 II surface as a catalyst (Fig. 7b).

Analyzing specific activity, k_{area}, against values of zeta potential, ζ_{pot}, a contradiction is found. More positive, ζ_{pot} should cause larger pollutant adsorption due to their carbonyl and carboxyl groups. Consequently, the order of activities would be expected to be CeO_2 III > CeO_2 I > CeO_2 II [22]. However, the observed order is CeO_2 II > CeO_2 I > CeO_2 III, increasing with the inverse of zeta potential $(\zeta_{pot})^{-1}$ (Fig. 7c). This fact suggests a different mechanism that cannot be explained exclusively by an adsorptive mechanism.

Another mechanism for explaining CeO_2-catalyzed ozonation considers the oxidation of the surface of catalyst by ozone as a first step. Just after surface oxidation by ozone, pollutant adsorbs on the catalyst and electrons are abstracted from the organic molecule, reducing the oxide surface and closing the catalytic cycle [34, 39] as shown in Fig. 8.

It is well known that Ce^{3+} and Ce^{4+} oxygen vacancies coexist on the surface of CeO_2. This can be understood as the energetic balance between the molar enthalpy of fluorite structure formation and redox potential Ce^{3+}/Ce^{4+}, $E^0 = 1.7$ V [39]. During CeO_2-catalyzed ozonation, oxidation of superficial Ce^{3+} occurs as the first step, leading to an unstable situation. Subsequently, electrons are abstracted from adsorbed organic molecules, reducing back superficial Ce^{4+} to Ce^{3+}. Therefore, activities of CeO_2 surfaces in catalyzed ozonation are closely correlated to superficial Ce^{3+} amounts [40, 41].

Luminescence spectra were used for an estimation of relative amounts of surface Ce^{3+}. Emission spectra of Ce^{3+} show the transition 5d $\rightarrow$ 4f. This transition is split into two bands at 380 and 480 nm due to spin–orbit coupling. The first one, at 380 nm, is split, also, into ten peaks due to crystal field stabilization of the lower $5d^1$ configuration [34] Ce^{4+} does not fluoresce in the UV/vis range. Figure 4 shows the spectra of the three oxide types. It could be verified that the intensities of luminescence and therefore the amounts of surface Ce^{3+} of oxides followed the sequence CeO_2 II > CeO_2 I > CeO_2 III. This fact agrees with the mechanism based on the redox properties of oxide surfaces, as schematized in Fig. 8.

These data suggest that, during the calcination of precursors, CeO_2 formation and citrate combustion compete for available oxygen. Therefore, Ce^{3+} amounts in the surface of oxides are directly linked to a reducing environment during calcination. In the precursor $[Ce_2(HCit)_3 \cdot 2H_2O]$, the

ratio citrate/Ce is 1.5; in [CeCit·xH_2O], it is equal to 1; and in [Ce(NO_3)Cit], the oxidative conditions are generated during calcination due to nitrate thermal decomposition which releases O_2 and N_2 and gives rise to a high oxygen condition.

Conclusions

The obtained data suggest that the adsorptive–oxidative mechanism of CeO_2-catalyzed ozonation is the more consistent explanation for the different activities showed by three CeO_2 types. In this way, Ce^{3+} would be the active site and the catalytic activities of CeO_2 vary with Ce^{3+} amounts at the surface of particles. Differences in surface Ce^{3+} amounts in the three oxides were attributed to demand of oxygen necessary for complete oxidation of citrates present in the precursors. So, for a higher organic content in the precursor, a higher activity of CeO_2 is observed in heterogeneous catalytic ozonation due to the presence of Ce^{3+} on the particle surface.

Acknowledgements M. F. Pinheiro da Silva thanks CAPES (Brazil) for a doctoral fellowship. We thank Prof. Dr. Márcia L. A. Temperini, for Raman spectra, Marilda M. G. R. Vianna for the use of thermal analysis instruments, Maria L. P. da Silva (EP-USP) for sputtering equipment, M. C. A. Fantini, F. M. S. Carvalho and M. J. Politi for the utilization of X-ray diffractometers. We also thank FAPESP (Grant 05/02745-7) for the BET equipment.

References

1. Raju B, Sivasankar BN. Spectral, thermal and X-ray studies on some new *Bis*-hydrazine lanthanide(III) glyoxylates. J Therm Anal Calorim. 2008;94:289–96.
2. Barry TK. The role of the lanthanides in the photonics, electronics and related industries. Inorg Chimica Acta. 1987;140:335–8.
3. Forster PL, Lugao AB, Brito HF, Parra DF. Calorimetric investigations of luminescent films polycarbonate (PC) doped with europium complex [Eu($TTA)_3(H_2O)_2$]. J Therm Anal Calorim. 2009;97:497–502.
4. Zhang T, Chen W, Ma J, Qiang Z. Minimizing bromate formation with cerium dioxide during ozonation of bromide-containing water. Water Res. 2008;42:3651–8.
5. Chockalingam R, Amarakoon VRW, Giesche H. Alumina/cerium oxide nano-composite electrolyte for solid oxide fuel cell applications. J Eur Ceram Soc. 2008;28:959–63.
6. Eom HJ, Choi J. Oxidative stress of CeO2 nanoparticles via p38-Nrf-2 signaling pathway in human bronchial epithelial cell. Toxicol Lett. 2009;1:77–83.
7. Wu X, Liang Q, Wu X, Weng D. Role of surface adsorption in fast oxygen storage/release of CeO-ZrO_2 mixed oxides. J Rare Earths. 2007;25:416–21.
8. Lin J, Kawai A, Nakajima T. Effective catalysts for decomposition of aqueous ozone. Appl Catal B. 2002;39:157–65.
9. Kaspar J, Fornasiero P, Graziani M. Use of CeO_2-based oxides in the three-way catalysis. Catal Today. 1999;50:285–98.
10. Yan M, Wei W, Zuoren N. Influence of pH on morphology and formation mechanism of CeO_2 nanocrystalline. J Rare Earth. 2007;25:53–7.
11. Zhang TM, Li J, Li H, Li Y, Shen W. Morphology-dependent redox and catalytic properties of CeO_2 nanostructures: nanowires, nanorods and nanoparticles. Catal Today. 2009;148:179–83.
12. Ge M, Guo C, Li L, Zhang B, Feng Y, Wang Y. Preparation of CeO_2 novel sponge-like rods by emulsion liquid membrane system and its catalytic oxidation property. Mat Lett. 2009;63:1269–71.
13. Shi DQ, Ionescu M, Silver TM, Dou SX. Relationship between epitaxial deposition and growth modes of CeO_2 films. Physica C. 2003;384:475–81.
14. Da Silva MFP, Carvalho FMS, Martins TS, Fantini MCA and Isolani PC, The role of citrate precursors on the morphology of lanthanide oxides obtained by thermal decomposition. J Therm Anal Calorim. 2009; doi: 10.1007/s10973-009-0380-1.
15. Kang ZC, Eyring L. A compositional and structural rationalization of the higher oxides of Ce, Pr, and Tb. J. Alloys Compd. 1997;249:206–12.
16. Zhang D, Zhang X, Ni X, Song J, Zheng H. Fabrication of novel threefold shape CeO_2 dendrites: optical and electrochemical properties. Chem Phys Lett. 2006;430:326–9.
17. Zhou K, Wang X, Sun X, Peng Q, Li Y. Enhanced catalytic activity of ceria nanorods from well-defined reactive crystal planes. J Catal. 2005;229:206–12.
18. Zheng X, Zhang X, Wang X, Wang S, Wu S. Preparation and characterization of CuO/CeO_2 catalysts and their applications in low-temperature CO oxidation. Appl Catal A. 2005;295:142–9.
19. Mahmoud A, Freire RS. Métodos emergentes para aumentar a eficiência do ozônio no tratamento de águas contaminada. Quim Nova. 2007;30:198–205.
20. Beltrán FJ, Rivas FJ, Montero-de-Espinosa R. Iron type catalysts for the ozonation of oxalic acid in water. Water Res. 2005;39:3553–64.
21. Gottschalk C, Libra AJ, Saupe A. Ozonation of water and wastewater. Weinheim: Wiley-VCH; 2000. p. 14.
22. Kasprzyk-Hordern B, Ziólek M, Nawrocki J. Catalytic ozonation and methods of enhancing molecular ozone reactions in water treatment. Appl Catal B. 2003;46:639–41.
23. Soeira LS, Freire RS, Catalytic ozonization: a new approach to the treatment of wastewater. In: Bakker SH, editors. Ozone depletion, chemistry and impacts. Hauppauge, Nova Science Publishers, Inc; 2009.
24. Da Silva MFP, Matos JR, Isolani PC. Synthesis, characterization and thermal analysis of 1:1 and 2:3 lanthanide (III) citrates. J Therm Anal Calorim. 2008;94:305–11.
25. Kosacki I, Suzuki T, Petrovsky V, Anderson HU, Colomban PH. Raman scattering and lattice defects in nanocrystalline CeO_2 thin films. Solid State Ion. 2002;149:99–105.
26. Karen P, Woodward PM. Liquid-mix disorder in crystalline solids: $ScMnO_3$. J Solid State Chem. 1998;141:78–88.
27. Brunauer S, Emmett PH, Teller E. Adsorption of gases in multimolecular layers. J Amer Chem Soc. 1938;60:3009–12.
28. Barret EP, Joyner LG, Halenda PH. The determination of pore volume and area distributions in porous substances. I. Computations from nitrogen isotherms. J Amer Chem Soc. 1951;73:373–5.
29. Smoluchowski M Three lectures on diffusion, Brownian motion and coagulation of colloidal carticles. Phys Z 1916;17:557–71, 585–99.
30. Standard Methods for the Examination of Water and Wastewater, 20th ed. CDIS: CD-ROM, 2003; 5310 B.
31. Standard Methods for the Examination of Water and Wastewater, 20th ed. CDIS: CD-ROM, 2003; 5530 C.

32. Qiu F, Pu X, Li J, Liu X, Pan Y, Guo J. Thermal behavior of the YAG precursor prepared by sol–gel combustion process. Ceram Int. 2005;31:663–5.
33. Brunauer S, Deming LS, Deming WS, Teller E. On a theory of van der Walls. J Am Chem Soc. 1940;62:1723–8.
34. Blasse G, Grabmaier BC, Lumin. Mat, Lewis PB, Leins J (Ed.), New York, 2002; 45-7.
35. Legube B, Leitner NKV. Catalytic ozonation: a promising advanced oxidation technology for water treatment. Catal Today. 1999;53:61–72.
36. Cooper C, Burch R. An investigation of catalytic ozonation for the oxidation of halocarbons in drinking water preparation. Water Res. 1999;33:3695–700.
37. Mvula E, Sonntag V. Ozonolysis of phenols in aqueous solution. Org Biomol Chem. 2003;1:1749–56.
38. Poznyk T, Vivero J. Degradation of aqueous phenol and chlorinated phenols by ozone. Ozone Sci Eng. 2005;27:447–58.
39. Vany′sek, P. In: Lide DR, editor. CRC handbook of chemistry and physics. 84th ed., CRC Press; 2004. pp 8–21.
40. Leitner BNKV. Catalytic ozonation: a promising advanced oxidation technology for water treatment. Catal Today. 1999;53:61–72.
41. Naydenov A, Stoyanova R, Mehandjiev D. Ozone decomposition and CO oxidation on CeO_2. J Mol Catal A. 1995;98:9–14.